A hybrid discrete–continuum framework for modelling filtration

I. M. Griffiths[a,*], P. S. Stewart[b]

[a]*Mathematical Institute, University of Oxford, Radcliffe Observatory Quarter, Oxford OX2 6GG, United Kingdom*
[b]*School of Mathematics and Statistics, University of Glasgow, G12 8QW, UK*

Abstract

Typical mathematical frameworks for modelling the blocking behaviour of a filter due to particle deposition fall into one of two categories: a continuum approximation, whereby particle deposition is assumed to occur in such a way that all pores in the material are in the same state of blocking at any given time; or a discrete model, where blocking is treated as individual events in both space and time. While the former is computationally inexpensive, the latter allows for variation from pore to pore. This pore-to-pore variation has been shown to provide a qualitative change in the observed filtration behaviour that is essential to reproduce experimental observations. We present a hybrid model that describes the location of particle depositions in a continuum manner while retaining a discrete, stochastic component to capture the time at which a blocking event occurs. The model is able to grade between the aforementioned extreme continuum and discrete cases through a parameter that controls the spatial extent of a blocking event. This enables us to uncover the way in which the nature of the blocking process changes between these two pre-existing models. The model also captures the key ingredients of a fully discrete stochastic model at a fraction of the computational cost, making it ready to use to describe other complex filtration scenarios.

1. Introduction

1.1. Motivation

Filtration is a vast industry with a wide range of applications, including water treatment [1], air purification [2], kidney dialysis [3] and food processing [4]. A filter may be thought of in simple terms as consisting of a network of interconnected pores. In dead-end filtration, a particle-laden fluid, or *feed*, is forced through the filter perpendicularly to the surface. If the particles are larger than the pores they can be sieved out on the filter surface (size exclusion); if they are smaller than the pores they penetrate into the filter depth where they may adhere to the pore walls or become lodged if the pores narrow or branch. Sieving, particle adhesion and internal trapping all lead to removal of the particles from the fluid, resulting in a fluid with a lower particle concentration than the input fluid.

The removal of particles comes at a cost, however. When the fluid is driven through the filter by a constant transmembrane pressure, as particles accumulate on the filter surface or adhere to the pore walls this leads to a reduction in the flux, with the total amount of fluid processed per unit membrane area, or *throughput*. The manner in which the flux falls with throughput is dependent on the type of filtration. For example, if the particles are being removed at the surface of the filter via size exclusion then the graph of flux, Q, versus throughput, V, observed experimentally is *convex*, *i.e.*, the second rate of change $Q''(V) > 0$, where primes denote differentiation [5] (figure 1a). However, if the particles are smaller than the pores and instead find their way into the internal pore structure before adhering to the pore walls to cause a constriction then the QV curves are concave: $Q''(V) < 0$ [6, 7, 8, 9] (figure 1b). As a result, QV curves are often used by practitioners to infer the type of blocking, or *fouling*, that the filter is experiencing without invasive methods.

Simple models to describe the surface deposition of particles assume that the particles form a layer of particles that is spatially uniform in thickness and that this layer provides an effective constant resistance per unit length to the flow. This model predicts a convex QV curve, in agreement with that observed in practice (see Appendix A.1 for a model derivation).

When modelling internal particle deposition, it is natural to make a similar assumption on spatial uniformity in the lateral direction, whereby at each instant in time all pores are assumed to be in the same state, with the

∗Corresponding author ian.griffiths@maths.ox.ac.uk

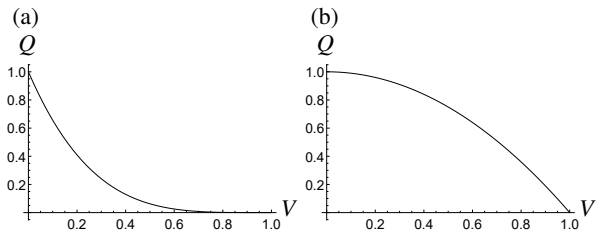

Figure 1: The two types of flux Q versus throughput V curves that arise when filtering particle-laden fluid through a filter under a constant transmembrane pressure difference. In (a) the QV curve is convex ($Q''(V) > 0$); this arises in idealized cases where the surface deposition or internal pore clogging is spatially uniform over the filter surface. In (b) the QV curve is concave ($Q''(V) < 0$); this arises in physical cases where the internal pore clogging occurs discretely, so that different pores may be in different states of blocking at any given time.

same number of particles deposited over the internal pore surface, with some given depth-dependent distribution. However, this model also predicts a convex QV curve, in contrast to that which is observed experimentally (see Appendix A.2 for a model derivation). One way in which concavity may be introduced into the QV models is by combining multiple fouling mechanisms. For example, a combination of pore blocking followed by cake-layer build-up was shown to describe the fouling of track-etched membranes by BSA [10] and proteins [11]. This approach can be generalized to other combinations of two fouling mechanisms [7] and has been further extended to capture three sequential fouling mechanisms, such as pore constriction followed by pore blocking and finally transitioning to deposition on the membrane surface, or *caking* [12].

Although more complex models are able to generate concave QV curves, these do not explain why the simple laterally invariant models describing a single fouling method cannot reproduce such concave curves despite the experimental evidence. The reason for this model failure was uncovered in [5], where it was shown that the deviations between the states of the different pores must be taken into account to correctly predict the QV curve. While this stochastic model satisfactorily resolves the modelling conundrum, it is then natural for one to query how relaxing the spatial uniformity of pore blocking leads to such a significant qualitative difference in the prediction. However, to date, the laterally invariant continuum models and discrete stochastic network models have remained distinct from one another. This is principally due to their fundamentally different frameworks: the assumption of lateral invariance affords a simple continuum description; allowing pores to be in different states of blocking lends itself to a discrete stochastic network model, which reproduces a broader range of physical experiments, but does not admit analytic solutions and is significantly more computationally expensive.

1.2. Continuum models

In the majority of continuum models, the pore structure is assumed to be homogeneous in the direction lateral to the flow. When the filter is undergoing internal deposition or caking, this is justified by assuming that all pores are in the same state of blocking at any given time. For scenarios in which complete blocking occurs, whereby a single particle will completely cover and blocks a pore, a model that tracks the average number of blocked pores per unit surface area is derived, which provides the equivalent laterally homogeneous description. In [13], the filtration of a feed solution comprising large particles that are trapped at the filter surface and small particles, which are trapped internally via adhesion to the pore walls is considered using a continuum approach. They model the microscale behaviour of a single pore and its constriction as particles adhere and identify the relevant upscaled continuum model of Darcy flow for the entire porous medium. This model assumes spatial homogeneity in the lateral direction. The authors examine how the performance may be improved by varying the pore radius with filter depth. By incorporating multiple blocking mechanisms they are able to obtain convex or concave QV curves. They show that a filter whose pore radius decreases with depth has a higher final throughput before reaching a threshold minimum flux and they find the constant porosity gradient that maximizes this throughput. This work is generalized in [14] to allow particles to become lodged internally.

In [15], the performance of a stack of filter materials of different porosities is examined. The flow is once again modelled in a continuum fashion using Darcy's law and the authors use the model to explore how changing the properties of the different layers can improve filtration performance. They find the optimal stack of filter porosities that maximize the final throughput of the filter.

Another branch of continuum methods for filtration involves the use of homogenization theory. Here, the microscale pore behaviour is formally upscaled to obtain a version of Darcy's equation and an advection–diffusion–reaction equation where the macroscale permeability, diffusivity, flow speed and reaction all couple to the microscale. In [16, 17], dead-end filtration is modelled for filters that possess a porosity gradient.

Again, it is assumed that the filter behaviour is independent of the direction lateral to the flow, and so a one-dimensional model is considered and used to understand how porosity gradients can improve filtration. In a similar manner to [13], they find that filters whose porosities decrease with depth lead to maximum throughput before blocking. They develop this further to find an analytic solution in the limit of slowly varying porosity gradients that corresponds to the porosity distribution that maximizes the contaminant removal and final throughput.

The effect of pore branching is studied in [18]. Here, while each pore is assumed to behave in an identical fashion, but the pore may branch asymmetrically and the concentration in the respective branches is tracked. One may think of this as a first step towards introducing lateral dependence to the flow problem. The branching structure allows for a porosity gradient and the effect of this on the efficiency of particle removal is studied. In a similar spirit to the aforementioned works, they find that a branching structure with pore radii that decrease with depth, so that the porosity decreases with depth, leads to a superior performance in terms of the amount of filtrate processed. They also show how this metric does not always align with a filter that removes the most particulates per unit volume of filtrate, demonstrating that one must be careful when setting the objective functions for optimization. This work is generalized in [19] where they show that allowing pore interconnectivity structures leads to higher total throughput before blocking.

1.3. Discrete network models

In discrete models for filters, the entire pore structure is modelled and blocking events are captured individually. Stochasticity is included straightforwardly, which naturally induces lateral dependence into the filter structure as blocking progresses. As mentioned in Section 1.1, in [5] it was shown that such pore-to-pore variation introduced by stochasticity is essential to describe the appropriate qualitative shape of flux-versus-throughput curves that match experimental observations. This work was generalized to address multiple layers of such membranes [20], which allows for porosity gradients. This provides the discrete stochastic analogue to [13, 14, 15]. The regular pore structure that was assumed in [5, 20] was relaxed in [21] to study a filter structure comprising a random array of interconnected pores, which more accurately describes a real porous filter. This provided a model to uncover the role played by the tortuosity of the various paths that the fluid must take through the filter on the resulting filtration efficiency.

1.4. Overview

In this paper we present a hybrid discrete–continuum framework that is able to reproduce the features of both a continuum description where all pores behave in the same way and a discrete network model and, more importantly, can transition between the two. Our model expresses the spatial properties of the filter in a convenient continuum manner while the particle transport process is modelled in a stochastic fashion. Such a model is desirable as it allows us to determine under what circumstances either of these two extreme versions of the model is required, and the underpinning physical changes that take place as we transition from one scenario to the other. These observations cannot be achieved by the purely continuum or purely discrete network models that have been studied so far. Moreover, this model provides a continuum framework that accurately captures the correct QV structure in a significantly more numerically efficient manner, with results that would take hours to simulate with a discrete stochastic network model being able to be reproduced in seconds.

In Section 2 we outline our new hybrid continuum modelling framework and the underlying assumptions. Our hybrid method is founded on the principles of a discrete network model where the spatial variation in the model is mapped to a continuum description. In Section 3 we show how one can continuously grade between a continuum description and a stochastic network model and show how the qualitative behaviour of a filter that follows these two models differs. We use the model to probe the variations in the pore constriction with depth and to subsequently explore the QV curves. We reveal self-similar dependence upon the parameters that characterize the deposition events, namely the spatial extent of a blocking event, the magnitude of that blocking event, and the likelihood of it taking place. We also uncover scaling laws on these model parameters. In Section 4 we discuss the mathematical implications, the physical significance of this work, and its potential future use in filtration science.

2. Modelling

We consider a filter set-up composed of a grid of interconnected circular pipes, or *pores*, with nodes (i, j) that are spaced a distance ΔL apart in both the x and y directions (see figure 2); we assume that the node spacing in the x and y directions are equal but our analysis

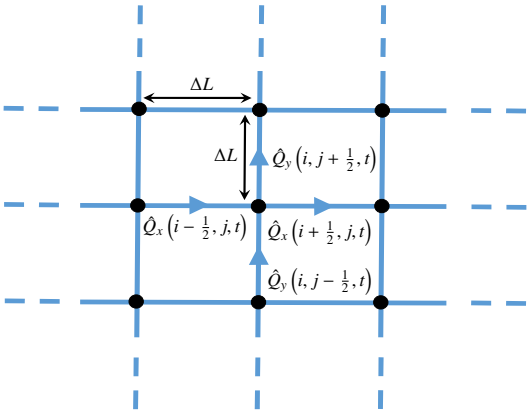

Figure 2: Schematic of the structure of the porous network under consideration and the associated nomenclature for the flow.

readily extends to different node separations. We denote the radius of the pore connecting nodes (i, j) and $(i+1, j)$ at time t by $\hat{a}_x(i+1/2, j, t)$ and the radius of the pore connecting nodes (i, j) and $(i, j+1)$ as $\hat{a}_y(i, j+1/2, t)$. We define the flux through these respective pores at this time as $\hat{Q}_x(i+1/2, j, t)$ and $\hat{Q}_y(i, j+1/2, t)$. These fluxes are related to the pore radii via Poiseuille's law [22]:

$$\hat{Q}_x\left(i+\tfrac{1}{2}, j, t\right) = \frac{\pi \hat{a}_x\left(i+\frac{1}{2}, j, t\right)^4 \left(\hat{p}(i, j, t) - \hat{p}(i+1, j, t)\right)}{8\mu\Delta L}, \quad (1a)$$

$$\hat{Q}_y\left(i, j+\tfrac{1}{2}, t\right) = \frac{\pi \hat{a}_y\left(i, j+\frac{1}{2}, t\right)^4 \left(\hat{p}(i, j, t)\right) - \hat{p}(i, j+1, t)}{8\mu\Delta L}, \quad (1b)$$

where $\hat{p}(i, j, t)$ is the pressure at node (i, j) at time t and μ is the viscosity of the fluid being filtered. Conservation of mass of the fluid at a point (i, j) gives

$$\hat{Q}_x\left(i+\tfrac{1}{2}, j, t\right) - \hat{Q}_x\left(i-\tfrac{1}{2}, j, t\right) + \hat{Q}_y\left(i, j+\tfrac{1}{2}, t\right) - \hat{Q}_y\left(i, j-\tfrac{1}{2}, t\right) = 0. \quad (2)$$

Dividing both sides of (2) by ΔL and taking the limit as $\Delta L \to 0$ gives the continuous equation for conservation of mass,

$$\nabla \cdot \boldsymbol{Q} = 0, \quad (3)$$

where $\nabla = (\partial/\partial x, \partial/\partial y)$ and $\boldsymbol{Q} = (Q_x, Q_y)$ is a continuum vector function of x, y and t such that $Q_x((i+1/2)\Delta L, j\Delta L, t) = \hat{Q}_\ell(i+1/2, j, t)$ and $Q_x(i\Delta L, (j+1/2)\Delta L, t) = \hat{Q}_y(i, j+1/2, t)$ as $\Delta L \to 0$. Similarly, taking the limit as $\Delta L \to 0$ in (1) gives

$$\boldsymbol{Q} = -\boldsymbol{a}^4 \otimes \nabla p, \quad (4)$$

where $\otimes$ denotes the outer product, $\boldsymbol{a} = (a_x, a_y)$ and p are continuum functions of x, y and t such that $a_x((i+1/2)\Delta L, j\Delta L, t) = \hat{a}_x(i, j, t)$, $a_y(i\Delta L, (j+1/2)\Delta L, t) = \hat{a}_y(i, j, t)$ and $p(i\Delta L, j\Delta L, t) = \hat{p}_\ell(i, j, t)$, for $\ell = x, y$, as $\Delta L \to 0$. Equation (4) is a version of Darcy's law with spatially varying permeability.

We consider a filter domain $(x, y) \in [0, L] \times [0, H]$. We assume that the inlet and outlet of the filter are located at $y = 0$ and $y = H$, respectively, and we apply a constant pressure difference ΔP across $0 \le y \le H$, which drives fluid through the filter; in the x-direction we assume periodicity:

$$p(x, 0, t) - p(x, L, t) = \Delta P, \quad (5a)$$

$$p(0, y, t) = p(L, y, t), \quad (5b)$$

$$\frac{\partial p(0, y, t)}{\partial x} = \frac{\partial p(L, y, t)}{\partial x}. \quad (5c)$$

We consider fluid entering the filter at $y = 0$ with a constant concentration of one particle per unit of fluid. The x location of particle insertion is selected stochastically with a probability based on the fluid flux through that part of the filter medium. Mathematically, the probability per unit width of a particle entering the filter medium at position x is given by

$$p_0(x, t) = \frac{Q_y(x, 0, t)}{\int_0^L Q_y(x, 0, t)\, \mathrm{d}x}. \quad (6)$$

The path of a particle through the filter is computed in discrete segments based on the steady flow field $\boldsymbol{Q}$. Each segment corresponds to a fixed timestep Δt, where the corresponding segment length (d) and orientation are computed based on the strength of and direction of the flow at that point. The particle then deterministically follows the direction of strongest flow. We note that the total path length can be used as a measure of tortuosity in an analogous manner to that considered in [21], although we do not explore this here.

We assign a probability p_a that the particle adheres per unit length of the filter medium it has traversed. Along each segment of the path, the probability of a particle adhering to the pore wall over is given by

$$p_t(d) = 1 - \mathrm{e}^{-p_a d}. \quad (7)$$

This feature is implemented numerically by generating a random number from a uniform distribution between 0 and 1 for each segment; if this random number is less than p_a then the particle is assumed to stick in this segment of the filter while otherwise it passes uninhibited.

When a particle deposits at a location (x_0, y_0) at time t we assume that the effect that the particle has on constricting the underlying pore radii is captured by a Gaussian distribution around that point:

$$a_\ell(x, y, t^+) = a_\ell(x, y, t^-) + A\left(\mathrm{e}^{-k((x-x_0)^2+(y-y_0)^2)} + \mathrm{e}^{-k((x-x_0-L)^2+(y-y_0)^2)} + \mathrm{e}^{-k((x-x_0+L)^2+(y-y_0)^2)}\right), \tag{8}$$

for $\ell = x, y$. The first Gaussian function corresponds to the deposition in $0 \le x \le L$ while the second and third Gaussian functions have the x location shifted by L in either direction to ensure that the deposition is periodic over $0 \le x \le L$. The parameter $k \ge 0$ provides a measure of the radial extent of the particle's influence upon deposition while A dictates the magnitude of the effect of the particle's adhesion on the pore constriction. We may identify A physically with the particle size. We accompany (8) by the initial condition

$$a(x, y, 0) = 1. \tag{9}$$

The function (8) captures the two extremes of particle modelling frameworks mentioned in the Introduction: when $k \to \infty$, the particles have a pointwise effect on the pore radius, which corresponds to discrete models such as those considered in [5, 20]; when $k = 0$, the particles affect the entire filter uniformly, which may be captured via a continuum description as shown in Appendix A.2. Note that one could easily introduce more complex blocking laws into the framework, such as those that depend on the pore radius. Such laws could account for additional physics such as the fact that smaller pores are likely to be constricted more than larger pores when a particle deposits (see, for example, [5] for such a physical blocking law). In principle, one might envisage conducting simple laboratory experiments to identify the relevant values of the parameters in (8) in order to quantitatively describe a specific filtration experiment. However, we emphasize that the specific form of (8) may change for different scenarios. Moreover, we have chosen this form simply since it conveniently embodies the key features that one would expect of a filter-blocking experiment and so may be used to demonstrate the abilities of the discrete–continuum framework.

With the blocking relationship (8), a_x and a_y will both change in the same way and so we only need to consider the function $a(x, y, t) \equiv a_x(x, y, t) = a_y(x, y, t)$. The function a then provides a measure of the pore radius. It would, however, be straightforward to consider scenarios in which the blocking mechanism in the pores in the x and y directions differed from one another by applying differing blocking relationships for a_x and a_y.

For the blocking law (8), the governing equation (4) reduces to

$$\boldsymbol{Q} = -a^4 \nabla p. \tag{10}$$

In our analysis, we will be interested in the cross-sectionally averaged outlet flux, defined by

$$\overline{Q}(t) = \int_0^L Q(x, H, t)\, \mathrm{d}x. \tag{11}$$

To facilitate comparisons for different parameter values, in our studies we apply a pressure difference ΔP for which $\overline{Q}(0) = 1$. We will be interested in how the average flux $\overline{Q}$ evolves with the total amount of fluid processed,

$$\overline{V}(t) = \int_0^t \overline{Q}(s)\, \mathrm{d}s. \tag{12}$$

We run the simulations until the flux $\overline{Q}$ first falls below a threshold value $\overline{Q}_{\text{final}}$. We define the final throughput, $\overline{V}_{\text{final}}$ to be the throughput when $\overline{Q} = \overline{Q}_{\text{final}}$. We will also be interested in the average pore radius,

$$\overline{a}(y, t) = \int_0^L a(x, y, t)\, \mathrm{d}x. \tag{13}$$

We solve the system (3), (8) and (10) numerically subject to the boundary conditions (5) and initial condition (9) using a finite-difference method. Here, spatial derivatives are discretized using centred second-order differences. We consider a domain of size $H = L = 1$ and for the cases presented in this paper we used 40 equally spaced grid internals in each direction. The flow is steady between particle-deposition events, so no time stepping is required. Note that p is unique up to an arbitrary constant in this system. However, here we will be concerned only with the fluid flux $\boldsymbol{Q}$ and so we do not need to specify the absolute value of the pressure. We run the simulations until $\overline{Q} = \overline{Q}_{\text{final}} = 0.01$. We repeat the simulation for each parameter configuration 20 times and present the average behaviour of all variables in our results, which smooths out the underlying stochastic nature of the process. The simulations are fast to run, taking less than a minute to complete all 20 simulations. This may be contrasted with the network models presented in [5] that take tens of minutes to run for domains of comparable size.

3. Results

3.1. The effect of the deposition radius, k

We first vary the parameter k in (8), which corresponds to varying the locality of the impact of the particle deposition. When $k = 0$ the particle deposition

occurs uniformly throughout the domain. This scenario may be directly identified with the spatially averaged continuum models (such as [13]) that assume that, at any instant in time, all pores are in the same state of blocking. In this case, equation (8) indicates that the pores will be constricted uniformly in space according to

$$\overline{a}(\overline{V}) = 1 - Ap_t(L)\overline{V} \tag{14}$$

as seen in figure 3(a). Note that this case is considered in Appendix A.2. We also show in Appendix A.2 the corresponding relationship if one were to assume that the pore radius shrinks uniformly across its depth a manner that preserves the total volume of deposited matter. As the value of k is increased, the effect of the particle deposition becomes progressively localized. When $k \neq 0$ the system no longer admits an analytic solution. The cross-sectionally averaged pore radius $\overline{a}$ now exhibits depth dependence, with the radius being lower closer to the inlet (figure 3b). This reflects the fact that more particles are likely to adhere closer to the inlet due to the probabilistic nature of the deposition. As k becomes larger, the pore radius falls even lower (figure 3b,c). A slight dip in the value of $\overline{a}$ also emerges, close to the inlet (figure 3b,c). This arises due to the fact that no particles deposit outside the filter domain, $y < 0$, and so the filter space near to the surface is influenced by the radial footprint of fewer particles.

We next move on to examine the flux–throughput profile, $\overline{Q}$ versus $\overline{V}$. When $k = 0$, substituting for $\overline{a}$ using (14) into (3) and (10) gives

$$\nabla^2 p = 0, \tag{15}$$

which, upon application of the boundary conditions (5) gives

$$p = -\frac{\Delta P}{L} y + \text{ constant}. \tag{16}$$

Substitution of this result into (10) and (11) and using the fact that $\overline{Q}(0) = 1$ gives

$$\overline{Q} = Q_y = \left(1 - Ap_t(H)\overline{V}\right)^4. \tag{17}$$

The expression (17) is convex $\left(\overline{Q}''\left(\overline{V}\right) > 0\right)$: the flux falls more slowly per unit of fluid processed in the later stages than the earlier part of the filtration process (figure 4a,b).

When we allow $k > 0$, the $\overline{QV}$ curves change nature, switching from convex to concave and becoming increasingly concave with increasing k (figure 4a,b); this means that the filter blocks more quickly with fluid processed. This corroborates the observation made in [5] that, when the local nature of particle deposition is taken into account, the $\overline{QV}$ curves are concave. In all cases

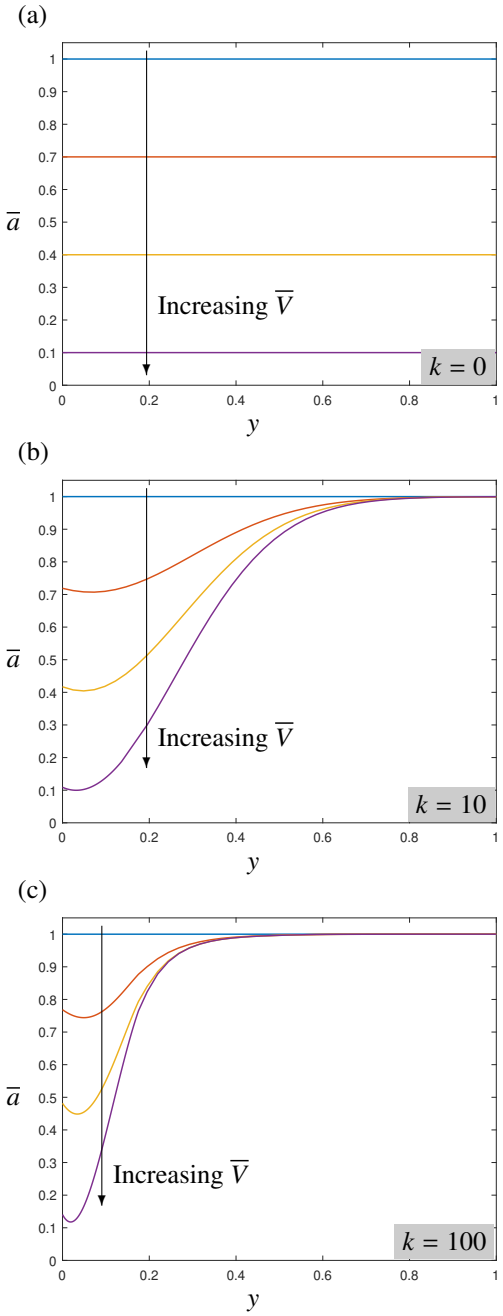

Figure 3: Mean pore radius $\overline{a}$ versus depth y for a deposition function given by (8) with $A = 0.01$, $p_a = 0.1$ and (a) $k = 0$ for $\overline{V} = 0, 10, 20, 30$, (b) $k = 10$ and $\overline{V} = 0, 55, 110$ and 165, and (b) $k = 100$ for $\overline{V} = 0, 200, 400$ and 600. The profiles in (a) are given analytically by (14).

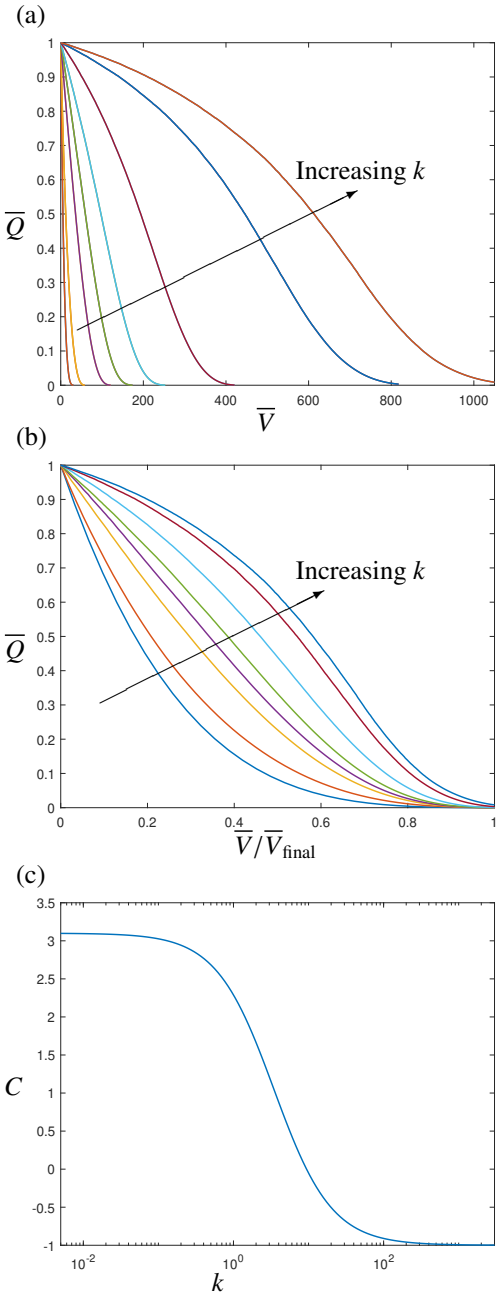

Figure 4: (a) Flux $\overline{Q}$ versus throughput $\overline{V}$ and (b) flux $\overline{Q}$ versus scaled throughput $\overline{V}/\overline{V}_{\text{final}}$ for a deposition function given by (8) with $A = 0.01$, $p_a = 0.1$ and $k = 0, 1, 5, 10, 20, 50, 150, 220$. The final throughput obeys the power law $\overline{V}_{\text{final}} \propto k^{\beta}$ for $\beta \approx 0.69$. The profile when $k = 0$ is given analytically by (17). (c) Curvature C, defined by (18), versus k.

though, a convex tail persists. A power law of the form $\overline{V}_{\text{final}} \propto k^{\beta}$ is obeyed for $\beta \approx 0.69$ when $A = 0.01$ and $p_a = 0.1$.

We can probe the nature of the $\overline{QV}$ curves further by investigating the curvature of the $\overline{QV}$ plots, which we define by

$$C = \overline{Q}''(\overline{V}/\overline{V}_{\text{final}}). \tag{18}$$

We use $\overline{V}/\overline{V}_{\text{final}}$ as the argument so that changes in C purely reflect changes in curvature rather than variations in $\overline{V}_{\text{final}}$. We determine the dependence of C on k by fitting a second-degree polynomial to $\overline{Q}$ versus $\overline{V}/\overline{V}_{\text{final}}$ for $0 \le \overline{V} \le \frac{1}{2}\overline{V}_{\text{final}}$ so that we determine the curvature in the first half of the evolution. For low values of k, the curvature is positive. As k increases the curvature falls, passing through zero when $k \approx 10$ before becoming negative. The curvature plateaus at a negative curvature as the $\overline{Q}$ versus $\overline{V}/\overline{V}_{\text{final}}$ curve converges to a self-similar solution as $k \to \infty$ (figure 4c).

As discussed in the Introduction, the curvature of a $\overline{QV}$ graph is often used in the filtration industry to infer the nature of the blocking phenomenon. As we highlighted, however, this curvature is dependent on whether we consider a model that assumes that blocking occurs uniformly across the cross-section of the filter medium or takes place as a local event. While models exist that describe the resulting $\overline{QV}$ behaviour in either case, here we have demonstrated how we can grade from one type of behaviour to the other in a continuous fashion and identify how the curvature changes continuously when we do so.

3.2. The effect of the deposition magnitude, A

We next turn our attention to the influence of the magnitude of the particle-deposition effect, characterized through the parameter A. As noted, we may identify this parameter with the particle size. As we would expect, when A is increased, the pore radius is reduced more quickly with throughput (figure 5). The curves of pore radius, a, versus filter depth, y, exhibit self-similar behaviour when plotted for the same values of $\overline{V}/\overline{V}_{\text{final}}$ for all values of k. Similarly, we find that the $\overline{QV}$ curves also exhibit self-similar behaviour with all plots of $\overline{Q}$ versus the scaled throughput $\overline{V}/\overline{V}_{\text{final}}$ collapsing onto a universal curve. This is true regardless of whether the $\overline{QV}$ curves are convex, for small values of k (figure 6a) or concave, for larger values of k (figure 6b). The final throughput follows an inverse relationship on A: $\overline{V}_{\text{final}} \propto A^{-1}$, emphasizing the linear manner in which A affects the radial pore constriction.

3.3. The effect of the probability of adhesion, p_a

When $k = 0$, the deposition location of a particle in the filter is irrelevant and so the pore radius will decrease uniformly in time regardless of the value of p_a

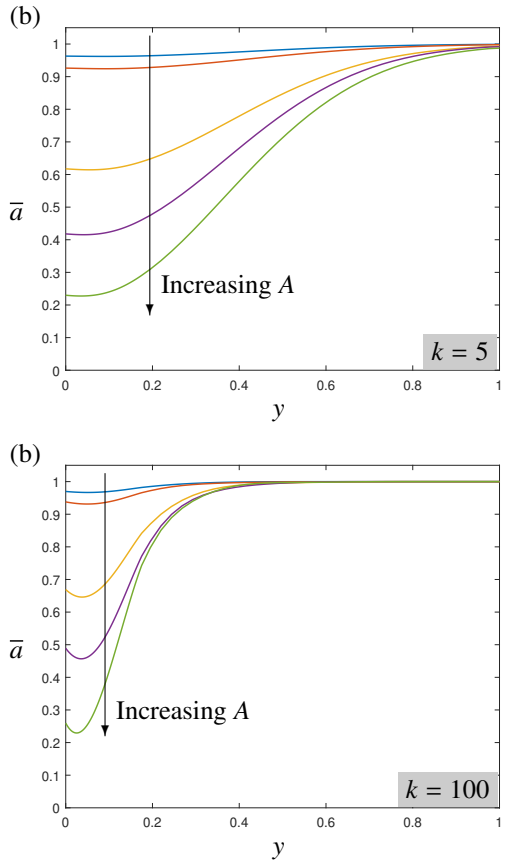

Figure 5: Mean pore radius $\overline{a}$ versus depth y for a deposition function given by (8) at $t = 50$ with $A = 0.005, 0.01, 0.02, 0.05, 0.075, 0.1$ and (a) $k = 5$ at $t = 10$ and (b) $k = 100$.

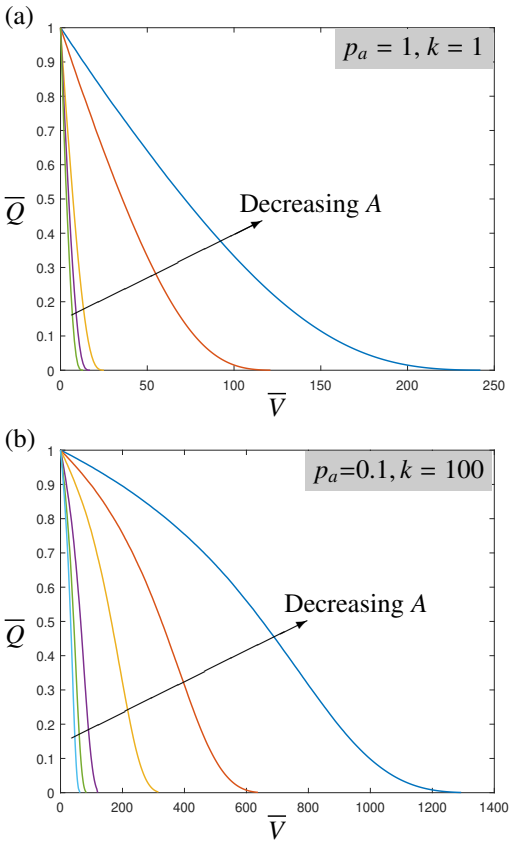

Figure 6: Flux $\overline{Q}$ versus throughput $\overline{V}$ for a deposition function given by (8) with $A = 0.001, 0.005, 0.01, 0.075$ and 0.1 and (a) $p_a = 1$ $k = 1$ and (b) $p_a = 0.1$, $k = 100$. In both cases, the curves are concave and broadly collapse with an inverse scaling relationship $\overline{V}_{\text{final}} \propto A^{-1}$. This self-similarity breaks down in the late stages of evolution in (b), where the curvature, C, defined by (18) becomes dependent on A: as A decreases, C increases. As A increases, C becomes negative.

(provided the particle deposits somewhere and does not pass entirely through the filter). When k is not too large so that each deposition has a finite but large radial extent, some spatial dependence begins to emerge in the pore radius versus depth (figure 7a). When k is large, and the deposition effect is highly localized, we observe a more pronounced effect when varying the probability of adhesion. As expected, as p_a is increased the pore radius falls more rapidly closer to the inlet (figure 7b). We observe an interior minimum of $\overline{a}$ in some cases. This arises due to two competing effects. First, the frequency of particle deposition falls with depth into the filter medium. This causes an increase in $\overline{a}$ with depth. Second, no particles are allowed to deposit outside of the filter medium, for $y < 0$. This means that a small neighbourhood near the filter inlet will experience the radial extent effect of fewer deposited particles than positions further into the depth. This corresponds to a rise in $\overline{a}$ as one gets closer to $y = 0$.

When $k = 0$, the $\overline{QV}$ curves will be unchanged as we vary p_a (again provided the particles deposit somewhere and do not pass through the entire filter). When k is not too large, an increase in the probability of adhesion leads to higher fluxes for the same throughput (figure 8a). This arises for the same reason as the interior minima in figure 7b): when the probability of deposition is higher, the particles are more likely to deposit closer to the inlet of the porous medium; this means that more of their region of influence will lie outside the porous domain and so they will have less of an overall effect on pore constriction. When k is large, and deposition is highly localized, we recover the more intuitive results that higher probabilities of adhesion lead to a faster decline in flux for sufficiently large k values (figure 8b). However, before this trend emerges, we observe the same effect as noted in figure 8(a), since to begin with particles are more likely to deposit nearer to the

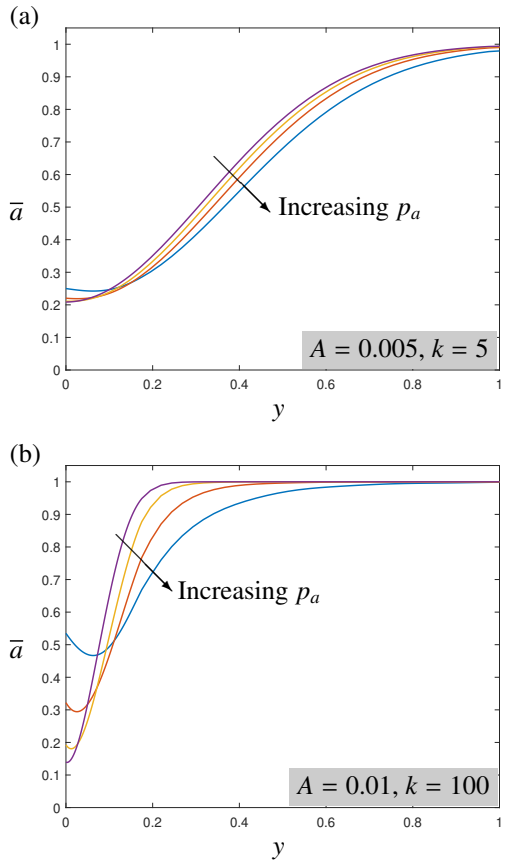

Figure 7: Mean pore radius $\overline{a}$ versus depth y for a deposition function given by (8) at $t = 500$ with $p_a = 0.05$, 0.1, 0.2 and 0.8 and (a) $A = 0.005$ and $k = 5$ at $t = 200$ and (b) $A = 0.01$ and $k = 100$ at $t = 500$.

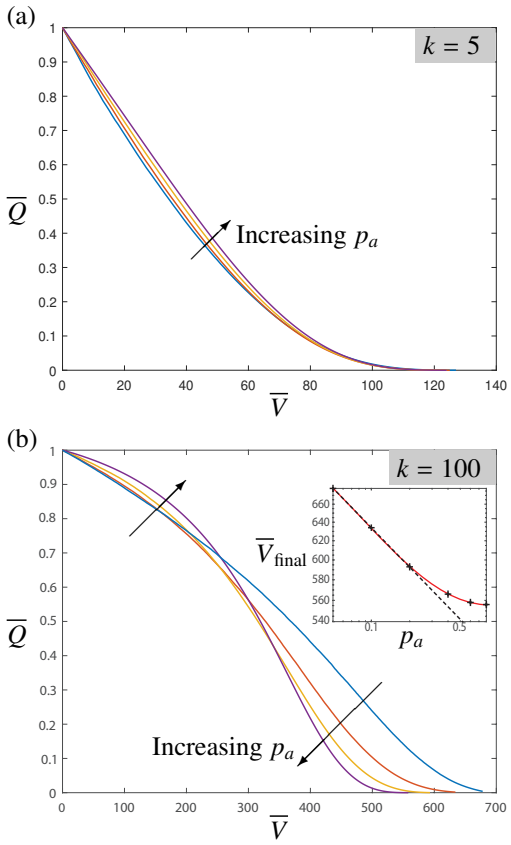

Figure 8: Flux $\overline{Q}$ versus throughput $\overline{V}$ for a deposition function given by (8) with $A = 0.01$ and $p_a = 0.05, 0.1, 0.2, 0.8$ with (a) $k = 5$ and (b) $k = 100$. When k is larger, an approximate power law of the form $\overline{V}_{\text{final}} \propto p_a^{\beta}$ with $\beta \approx -0.088$ is obeyed for smaller values of p_a but deviates from this when p_a becomes larger (inset of b, dashed line). The red curve in the inset is to guide the eye.

surface for higher p_a values, where more of their radius of influence lies outside the filter domain. These two combined features lead to a crossover in the $\overline{QV}$ curves. The final throughput $\overline{V}_{\text{final}}$ obeys a weak power-law dependence on p_a of the form $\overline{V}_{\text{final}} \propto p_a^{\beta}$ with $\beta \approx -0.088$ for low values of p_a. However, this relationship breaks down as p_a becomes larger (see inset of figure 8b).

4. Conclusions

In this paper we proposed a hybrid discrete–continuum framework to describe the blocking process in a filter as particle-laden fluid is passed through. Our novel framework bridges the gap between the two extreme limits that currently exist in the literature: a continuum model where all pores behave in the same way (e.g., [13]) and a discrete model where each blocking event is captured individually (e.g., [5]). Particle depositions are captured via a continuous description in space and discretely in time. The model is able to grade between the two extreme cases by varying a single parameter that corresponds to the radial extent of a particle deposition. This enabled us to show how the two models differ in their qualitative predictions for internal pore blocking: a continuum description predicts convex $\overline{QV}$ curves while a discrete model predicts concave $\overline{QV}$ curves. Moreover, the model shows how the $\overline{QV}$ curves depend on the radial extent of a deposition (figure 4). We were also able to reveal the dependence of flux decline on the magnitude of a deposition event (figure 6) and its probability of occurrence (figure 8). We uncovered self-similarity that allows the data to collapse onto universal curves, as well as scaling-law dependence of the system performance on the key parameters.

The model we proposed readily generalizes in a variety of ways. First, one may generalize the network structure to allow for pores that differ in length depending on the location in the filter (in a suitably slowly vary-

ing way to enable the continuum limit to be taken). This would result in the divergence term in the governing equation (3) being replaced with a space-dependent gradient operator. Second, we chose to consider a porous material whose pore structure is initially spatially uniform. This may be modified to consider an initial pore structure with spatial dependence. For instance, one might be interested in exploring how a porosity gradient can improve filtration performance. The discrete version of this problem has been studied in [20] while a continuous version derived using homogenization theory has been examined in [16, 17].

One of the main generalizations of this model comes in the form of the deposition law. Here, we chose a simple law in which each deposition event had the same effect on the underlying material, (8). In many cases though, deposition may depend on the underlying pore structure or the position if the filter is composed of different materials. Such effects can easily be incorporated by replacing (8) with the appropriate constitutive law.

The model framework itself may be generalized by relaxing the assumption of a square (or rectangular) grid, as is more likely to be observed in real-life filters. One could envisage constructing a random network by sampling each pore length from a distribution with mean and standard deviation as done in [21]. By ensemble averaging over a series of such filter geometries one could then obtain the effective behaviour of a real-life filter. This is beyond the scope of this paper but clearly a route of interest as we focus our efforts on modelling increasingly realistic pore constructions that may be provided, for example, from scanning electron microscopy (SEM) images.

The method we present here is able to replicate the flux decline that is observed in practice and captured by a fully discrete model, but at a fraction of the computational cost; typical simulations take less than a minute rather than tens of minutes. The framework is thus prime for deployment to describe other complex filtration scenarios where it should allow practitioners to probe the experimental field and offer key insight into future filter design.

Appendix A. Flux models

In this section we model the flux decline for surface deposition (caking) or internal pore deposition where we assume that the fouling mechanism occurs uniformly across the filter cross-section so that the problem is laterally invariant.

Appendix A.1. Caking

The filter will offer a resistance to the flow, say R_m. If a uniform layer of particles builds up on the surface of the filter, this will add an additional resistance, R_c, which is proportional to the thickness of the layer of particles, or the *cake*. Since particles arrive with every unit of fluid flux, the resistance of the cake layer will rise linearly with flux: $R_\mathrm{c} = \gamma\overline{V}$, where $\gamma > 0$ is a constant related the size of the particles and how closely they pack. The flux of fluid through the filter and cake combination is given by $\overline{Q} = \sigma/(R_\mathrm{m} + R_\mathrm{c})$ where σ is another constant related to the geometry of the underlying porous structure. The associated curvature is thus $C = \overline{Q}''(V) = 2\sigma\gamma^2/(R_\mathrm{m} + \gamma V)^3 > 0$ and so the $\overline{QV}$ curve is convex.

Appendix A.2. Internal pore deposition

Next we consider internal deposition in a filter composed of straight cylindrical pores that span the entire thickness of the filter. We assume that all pores experience identical blocking so that at any given instant in time each pore is in the same state of constriction. For simplicity and illustrative purposes, here we assume that particles deposit uniformly over the length of the pore but our derivation generalizes to account for depth-dependent adhesionin the same manner. As the pore constricts, the flow will reduce according to Poiseuille's law, (1). This gives

$$\overline{Q} = \frac{N\pi a(V)^4 \Delta P}{8\mu L}, \tag{A.1}$$

where N is the number of pores per unit membrane area. In the case considered in this paper, particle deposition shrinks the pore radius independently of the current state (equation (8)). This means that $a'(V) < 0$ and $a''(V) = 0$. In this case, the curvature,

$$C = \overline{Q}''(V) = \frac{3\pi a^2 \Delta P (a')^2}{\mu L} > 0 \tag{A.2}$$

and so the $\overline{QV}$ curve is, again, convex.

An alternative common scenario is to assume that the pore radii shrink uniformly in response to deposition in a manner that preserves the total volume of material that has deposited. In this case,

$$a(V) = \sqrt{a(0)^2 - \frac{4r^3 V n}{3L}} \tag{A.3}$$

where r is the particle radius and n is the number of particles per unit volume of fluid in the feed. In this

case, (A.1) gives

$$\overline{Q} = \frac{\pi \Delta P}{8\mu L}\left(a(0)^2 - \frac{4r^3 V n}{3L}\right)^2 \tag{A.4}$$

and so

$$C = \frac{4\pi \Delta P n^2 r^6}{9\mu L^3} > 0 \tag{A.5}$$

and so the curve is also convex in this case.

Acknowledgements

IMG gratefully acknowledges support from the Royal Society through a University Research Fellowship.

References

[1] A. Zularisam, A. Ismail, R. Salim, Behaviours of natural organic matter in membrane filtration for surface water treatment—a review, Desalination 194 (2006) 211–231.
[2] R. C. Brown, Air filtration: an integrated approach to the theory and applications of fibrous filters (1993).
[3] H. Lonsdale, The growth of membrane technology, Journal of Membrane Science 10 (1982) 81–181.
[4] G. Daufin, J.-P. Escudier, H. Carrère, S. Bérot, L. Fillaudeau, M. Decloux, Recent and emerging applications of membrane processes in the food and dairy industry, Food and Bioproducts Processing 79 (2001) 89–102.
[5] I. M. Griffiths, A. Kumar, P. S. Stewart, A combined network model for membrane fouling, Journal of Colloid and Interface Science 432 (2014) 10–18.
[6] A. Grenier, M. Meireles, P. Aimar, P. Carvin, Analysing flux decline in dead-end filtration, Chemical Engineering Research and Design 86 (2008) 1281–1293.
[7] G. Bolton, D. LaCasse, R. Kuriyel, Combined models of membrane fouling: Development and application to microfiltration and ultrafiltration of biological fluids, Journal of Membrane Science 277 (2006) 75–84.
[8] C. Duclos-Orsello, W. Li, C.-C. Ho, A three mechanism model to describe fouling of microfiltration membranes, Journal of Membrane Science 280 (2006) 856–866.
[9] Y. S. Polyakov, Depth filtration approach to the theory of standard blocking: Prediction of membrane permeation rate and selectivity, Journal of Membrane Science 322 (2008) 81–90.
[10] C.-C. Ho, A. L. Zydney, A combined pore blockage and cake filtration model for protein fouling during microfiltration, Journal of Colloid and Interface Science 232 (2000) 389–399.
[11] L. Palacio, C.-C. Ho, A. L. Zydney, Application of a pore-blockage—cake-filtration model to protein fouling during microfiltration, Biotechnology and Bioengineering 79 (2002) 260–270.
[12] C. Duclos-Orsello, W. Li, C.-C. Ho, A three mechanism model to describe fouling of microfiltration membranes, Journal of Membrane Science 280 (2006) 856–866.
[13] P. Sanaei, L. J. Cummings, Flow and fouling in membrane filters: effects of membrane morphology, Journal of Fluid Mechanics 818 (2017) 744–771.
[14] P. Sanaei, L. J. Cummings, Membrane filtration with multiple fouling mechanisms, Physical Review Fluids 4 (2019) 124301.
[15] D. Fong, L. Cummings, S. Chapman, P. Sanaei, On the performance of multilayered membrane filters, Journal of Engineering Mathematics 127 (2021) 1–25.
[16] M. P. Dalwadi, I. M. Griffiths, M. Bruna, Understanding how porosity gradients can make a better filter using homogenization theory, Proceedings of the Royal Society A 471 (2015) 20150464.
[17] M. P. Dalwadi, M. Bruna, I. M. Griffiths, A multiscale method to calculate filter blockage, Journal of Fluid Mechanics 809 (2016) 264–289.
[18] P. Sanaei, L. J. Cummings, Membrane filtration with complex branching pore morphology, Physical Review Fluids 3 (2018) 094305.
[19] B. Gu, D. Renaud, P. Sanaei, L. Kondic, L. Cummings, On the influence of pore connectivity on performance of membrane filters, Journal of Fluid Mechanics 902 (2020).
[20] I. M. Griffiths, A. Kumar, P. S. Stewart, Designing asymmetric multilayered membrane filters with improved performance, Journal of Membrane Science 511 (2016) 108–118.
[21] I. M. Griffiths, I. Mitevski, I. Vujkovac, M. R. Illingworth, P. S. Stewart, The role of tortuosity in filtration efficiency: A general network model for filtration, Journal of Membrane Science 598 (2020) 117664.
[22] H. Ockendon, J. R. Ockendon, Viscous Flow, Cambridge University Press, 1995.